

# Tailoring the Oxygen Reduction Activity of Pt Nanoparticles through Surface Defects: A Simple Top-Down Approach

Johannes Fichtner,<sup>▼</sup> Sebastian Watzel,<sup>▼</sup> Batyr Garlyyev, Regina M. Kluge, Felix Haimerl, Hany A. El-Sayed, Wei-Jin Li, Frédéric M. Maillard, Laetitia Dubau, Raphaël Chattot, Jan Michalička, Jan M. Macak, Wu Wang, Di Wang, Thomas Gigl, Christoph Hugenschmidt, and Aliaksandr S. Bandarenka\*

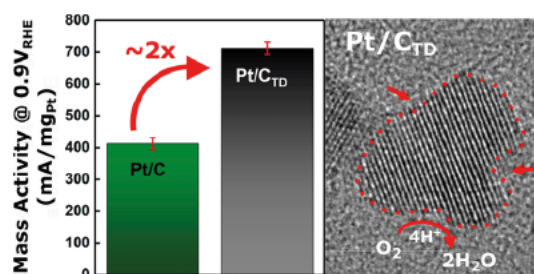
**ABSTRACT:** Results from Pt model catalyst surfaces have demonstrated that surface defects, in particular surface concavities, can improve the oxygen reduction reaction (ORR) kinetics. It is, however, a challenging task to synthesize nanostructured catalysts with such defective surfaces. Hence, we present a one step and upscalable top down approach to produce a Pt/C catalyst (with  $\sim 3$  nm Pt nanoparticle diameter). Using high resolution transmission electron microscopy and tomography, electrochemical techniques, high energy X ray measurements, and positron annihilation spectroscopy, we provide evidence of a high density of surface defects (including surface concavities). The ORR activity of the developed catalyst exceeds that

of a commercial Pt/C catalyst, at least 2.7 times in terms of specific activity ( $\sim 1.62$  mA/cm<sup>2</sup><sub>Pt</sub> at 0.9 V vs the reversible hydrogen electrode) and at least 1.7 times in terms of mass activity ( $\sim 712$  mA/mg<sub>Pt</sub>), which can be correlated to the enhanced amount of surface defects. In addition, the technique used here reduces the complexity of the synthesis (and therefore production costs) in comparison to state of the art bottom up techniques.

**KEYWORDS:** electrocatalysis, fuel cell, oxygen reduction, platinum nanoparticles, top down synthesis

## INTRODUCTION

With the increased awareness of preventing climate change, efforts are being made to decouple our society's energy demands from the so called carbon cycle. One promising approach is to reduce emissions caused by automotive combustion engines, for instance by replacing this technology with electric motors that are powered by batteries and/or hydrogen fuel cells.<sup>1,2</sup> Even though the market launch of hydrogen fuel cell driven cars is on the rise, further cost reductions are required to make the technology commercially more competitive. Today, the anode and cathode catalyst layers of proton exchange membrane fuel cells (PEMFCs) typically consist of Pt based nanostructures supported on high surface area carbon (Pt/C).<sup>3</sup> While the hydrogen oxidation reaction taking place at the anode side of the cell is a rapid process, the oxygen reduction reaction (ORR) at the cathode side exhibits sluggish kinetics. In order to improve the activity of such catalysts, two approaches are typically pursued. One way is to alloy Pt nanoparticles with less precious transition metal elements (e.g., Co, Ni, Cu) or lanthanides (e.g., Pr),<sup>4–7</sup> which alters the electronic properties of the catalyst surface by a combination of so called “strain” and “ligand” effects. This weakens the strong surface–intermediate interactions and allows optimization of electron transfer.<sup>8,9</sup> In particular, both



Pt<sub>3</sub>Ni bulk and nanoscale alloy structures notably exceeded the activity of pure Pt.<sup>10–12</sup> However, due to the dissolution of the solute metal during PEMFC operation (commonly known as “dealloying”), the membrane electrode assembly can get poisoned, resulting in poor long term performance.<sup>13</sup> Another promising approach is to directly alter the catalytic properties of Pt nanoparticles by the modification of their surface structure. For example, tailoring the size of the nanoparticles and the design of unusual catalyst shapes with enhanced surface area (e.g., hollow nanoparticles, aerogels) can be mentioned.<sup>14–16</sup> Importantly, in such cases the increased activity toward the ORR can, among others, also be attributed to the generation of highly active defectlike surface sites. In particular, Calle Vallejo et al. demonstrated that surface concavities on Pt significantly improve ORR kinetics.<sup>17,18</sup> This is due to the optimized geometric structure at the concave sites, as quantified by the so called generalized coordination number ( $\overline{CN}$ ) approach. Particularly high  $\overline{CN}$  values have been

predicted for e.g. hollow or coalescing nanoparticles at their boundary, confirming the aforementioned experimental findings. Furthermore, the activity of concave shaped nanocubes was experimentally demonstrated by Yu et al.,<sup>19</sup> but the degree of negative curvature was not very pronounced and the size of the concave nanocubes was larger than 20 nm, which results in low mass activity. Furthermore, the development of a simple production method for such concave nanoparticles often is a nontrivial endeavor. Current research has mainly focused on the synthesis of such catalysts using conventional bottom up techniques, which typically suffer from complex and time consuming multiple step procedures.<sup>20</sup> Hence, the development of a facile synthetic method for Pt nanostructures, which contain these active sites, is a crucial step toward the commercial realization of PEMFC driven cars on a large scale. Here, we take advantage of a novel top down synthetic route, in order to prepare Pt/C catalysts with a high degree of surface defects. This top down approach, which was initially discovered decades prior to the beginnings of nanotechnology and introduced as atomization of metal cathodes,<sup>21</sup> uses high alternating anodic and cathodic biases applied to metal wires immersed in an alkaline electrolyte, in order to produce nanoparticles at the electrode surface and subsequently release them into the electrolyte. Fundamental experiments on the nanoparticle synthesis by this approach were provided by the groups of Koper, Li, and Bandarenka in recent years and extended to different types of noble and non noble metals as well as alloys and oxide materials.<sup>22–26</sup> With the help of high resolution transmission electron microscopy (HR TEM), high resolution scanning transmission electron microscopy with a high angle annular detector (HR STEM HAADF), STEM HAADF tomography visualization, Rietveld refinement of wide angle X ray scattering (WAXS), electrochemical techniques, and positron annihilation spectroscopy (PAS), we provide evidence that the top down synthesis leads to the formation of Pt nanoparticles with rough, disordered surfaces. In particular, this includes surface concavities. Furthermore, utilizing the rotating disk electrode (RDE) technique and single cell PEMFC measurements, we show that Pt/C produced by this top down approach (denoted as Pt/C<sub>TD</sub> in the following) is indeed highly active toward the ORR.

## EXPERIMENTAL SECTION

**Synthesis.** In a typical synthesis of Pt/C<sub>TD</sub>, 20 mg of Vulcan XC72R active carbon (Cabot, USA) was dispersed in 25 mL of a 1 M KOH (85%, Grüssing, Germany) solution. To improve the wettability of the carbon support, ~100  $\mu$ L of ethanol (puriss, >99.8%, Sigma Aldrich, Germany) was added to the suspension, followed by sonication for 15 min. Subsequently, two Pt wires (99.999%, Goodfellow, Germany) with a diameter of ~0.2 mm were connected as electrodes and immersed in the suspension with vigorous stirring. To produce Pt nanoparticles, a sinusoidal potential of  $\pm 10$  V vs Pt pseudoreference (frequency 200 Hz) was applied, leading to the erosion of the Pt wires. After generation of the demanded Pt weight fraction, the suspension was stirred for 12 h at room temperature, followed by filtering, washing with ultrapure water (Evoqua, Germany), and drying in the oven at 60 °C. As a reference catalyst, TEC10V20E Pt/C (19.6 wt %) from Tanaka Kikinokogyo (Pt/C<sub>TKK</sub>) was used without further modification.

**Pt on Carbon Weight Fraction.** The weight fraction of Pt<sub>TD</sub> nanoparticles on carbon was determined using

thermogravimetric analysis (TGA). The measurements were carried out with a Mettler Toledo TG MS coupling instrument with an air flow of 50 mL/min and heating speed of 50 K/min to 1100 °C. Prior to ramping of the temperature, the sample was dried at ~135 °C, followed by a determination of its initial weight. Before it was cooled, the sample was kept at 1100 °C for 50 min until no further weight loss could be observed. The mass was compared after cooling to 135 °C.

**Electron Microscopy.** For TEM imaging of the Pt/C<sub>TD</sub> electrocatalyst, a Philips CM100 EM instrument, operated at 100 kV, was used. The samples were prepared by sonicating the catalyst powder in isopropanol, followed by drop casting the dispersion on Formvar supported carbon coated Cu400 TEM grids (Science Services, Germany). HR (S)TEM imaging of the unsupported Pt<sub>TD</sub> nanoparticles was conducted on a TITAN Themis 60 300 instrument (ThermoFisher Scientific, USA) operated at 300 kV and equipped with a Schottky FEG type emission gun, a spherical aberration corrector for the objective lens, and HAADF detector (Fischione, USA). The TEM sample of the unsupported Pt<sub>TD</sub> nanoparticles was prepared from Pt nanoparticles dispersed in ultrapure water by sonication for 15 min, which were immediately dripped on a copper TEM grid with a quantifoil holey carbon membrane covered by graphene oxide. The HR TEM and HR STEM images were acquired using the software Velox v.2.6 (Thermo Fisher Scientific, USA), and Fourier filtering was performed using masks on selected spots in fast Fourier transformation (FFT) patterns in the software Digital Micrograph GSM 2 (Gatan Inc., USA). The tomography of the unsupported Pt<sub>TD</sub> nanoparticles was conducted on a TITAN 80 300 instrument (FEI Company, USA) operated at 300 kV in STEM mode using the HAADF detector, which allows imaging with high contrast between Pt nanoparticles and the carbon membrane of the TEM grid. The same sample as for TEM analysis (described above) was used, but round Au tracking nanoparticles (diameter ~6.5 nm), dispersed in high purity water, were dripped on the grid additionally to allow later alignment of the images in the whole tilting range. The tilting range used was  $\pm 72^\circ$ , and the STEM HAADF images were taken in  $2^\circ$  steps. A 2020 high field of view single tilt tomography holder (Fischione, USA) was used for the tomography tilt series acquisition. The tomography data were obtained using the corresponding STEM tomography data acquisition software v.4.1 (ThermoFisher Scientific, USA) with automatic and dynamic focusing. The postprocessing of the tomography data consisted of three parts: alignment, reconstruction, and visualization. The alignment was performed using the open source software IMOD v.4 (University of Colorado, USA) with plugin eTomo, where a fiducial model was created by manual tracking of Au beads surrounding the structure of interest with a residual error of the alignment of 1.2 pixel. The reconstruction was performed using the software Inspec3D v.3.1 (FEI Company, USA) from the previously aligned data set, and a 3D volume of the desired size was created. The final colorful visualization of the reconstructed volume was performed using the software AMIRA (ThermoFisher Scientific, USA).

**Electrochemical Measurements.** Electrocatalytic activity measurements were performed using a standard electrochemical cell, filled with 0.1 M HClO<sub>4</sub> (Suprapur, Merck, Germany) as electrolyte. The cell was frequently cleaned with a 3/1 mixture of sulfuric acid and hydrogen peroxide, followed by boiling the cell with ultrapure water. Electrochemical

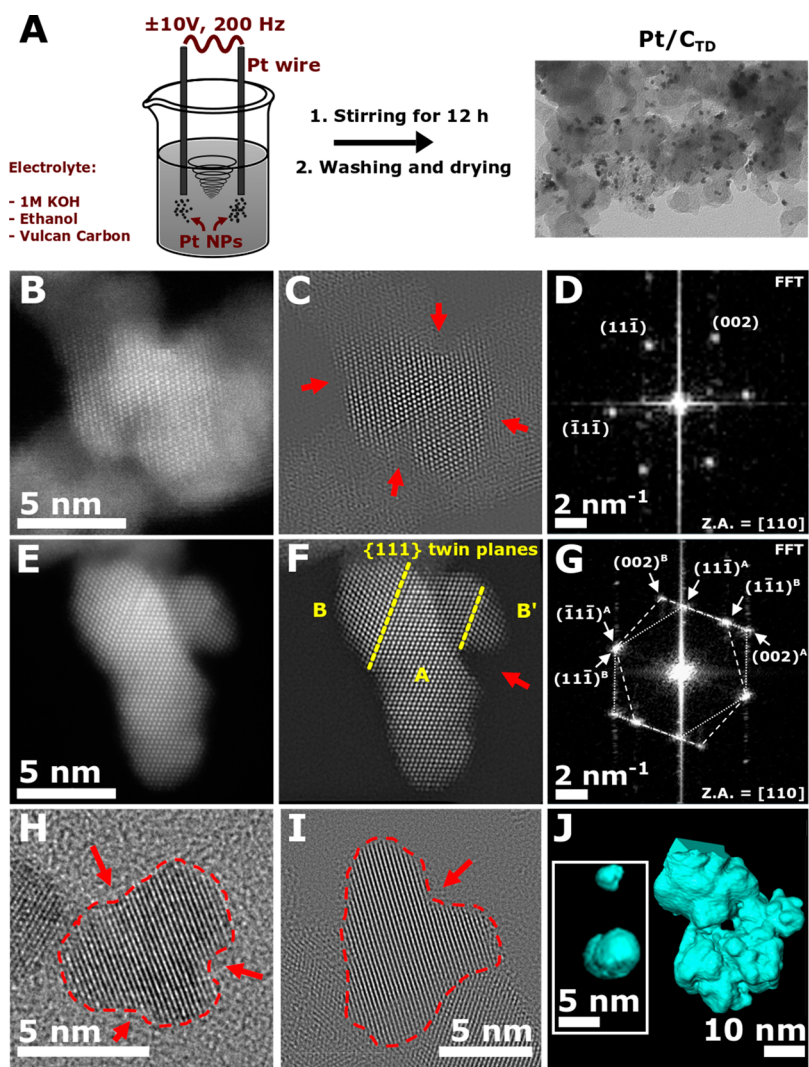


**Figure 1.** (A) Schematic description of the synthetic procedure toward the Pt/C<sub>TD</sub> electrocatalyst. Application of an alternating sinusoidal potential ( $\pm 10$  V, 200 Hz) to Pt wires immersed in a suspension of Vulcan carbon in 1 M KOH and ethanol with vigorous stirring leads to the formation of carbon supported Pt nanoparticles. (B, E) HR STEM images of unsupported Pt<sub>TD</sub> single nanoparticles with corresponding (C, F) Fourier filtered images and (D, G) FFT patterns (Z.A. = zonal axis). Certain concavities are highlighted by red arrows. Twin boundaries and twin grains A, B, B' are marked in (F). (H, I) HR TEM images of unsupported Pt<sub>TD</sub> nanoparticles. Concave regions are highlighted by red arrows. (J) 3D visualization of two unsupported, single Pt<sub>TD</sub> nanoparticles, as well as a fraction of unsupported nanoparticle agglomerate, using STEM HAADF tomography. Several concave regions are visible on both the individual and the agglomerated nanoparticles.

measurements were conducted using a BioLogic VSP 300 (BioLogic, France) potentiostat. As a substrate for Pt/C<sub>TD</sub>, a glassy carbon electrode with a diameter of 5 mm and an area of 0.196 cm<sup>2</sup> (Pine Instruments, USA) in combination with a Pine MSR electrode rotator (Pine Instruments, USA) was used. For electrochemical studies, freshly prepared catalyst inks were used. A typical catalyst ink ratio consisted of  $\sim 10$  mg finely ground catalyst powder, 3.6 mL of ultrapure water, 1.466 mL of isopropanol (puriss, >99.8%, Sigma Aldrich, Germany), and 0.03 mL of Nafion dispersion (5 wt % in lower aliphatic alcohols and water, Sigma Aldrich, Germany). To obtain a homogeneous dispersion, the inks were sonicated for 20 min prior to their first use. Prior to use, the electrode was polished with alumina paste (1.0, 0.3, and 0.05  $\mu$ m) and rinsed with ultrapure water. A commercial mercury/mercurous sulfate electrode (0.6M K<sub>2</sub>SO<sub>4</sub>, Schott, Germany) served as the reference electrode. A Pt wire (99.9%, Goodfellow, Germany) served as the counter electrode. It has to be noted that CO

stripping voltammetry was recorded in a slightly modified setup. As a reference electrode, a commercial Hydroflex hydrogen electrode (Gaskatel, Germany) was utilized. Experiments were operated with an Autolab PGSTAT302N potentiostat (Metrohm, France).

**Membrane Electrode Assembly Measurements.** Single cell PEMFC measurements were conducted with a homemade cell setup. The fuel cell performance was evaluated on a Greenlight Innovation G60 test station (Greenlight Innovation Corp., Canada), coupled with a Gamry reference 3000 potentiostat (Gamry Instruments, USA). Five square centimeter catalyst layers were prepared using the decal transfer method, i.e. by rod coating on a PTFE decal, followed by drying at room temperature. As the anode catalyst, commercial Pt/C<sub>TKK</sub> (TEC10 V20E) with an anode loading of 0.08 mg<sub>Pt</sub>/cm<sup>2</sup> was used. As the cathode catalyst, Pt/C<sub>TD</sub> with a cathode loading of 0.1 mg<sub>Pt</sub>/cm<sup>2</sup> was utilized. The synthesis of Pt/C<sub>TD</sub> electrocatalyst was conducted as described

in the previous sections; however, the batch size was increased from ~20 to ~100 mg of Pt/C<sub>TD</sub>. For ink preparation, the catalyst was dispersed in a mixture of 1 propanol and water (~10 wt %) and the ionomer (Nafion, 5 wt % in lower aliphatic alcohols and water, Sigma Aldrich, Germany) to carbon (I/C) ratio was adjusted to 0.65. The ink was mixed on a roller mill for 18 h at room temperature, using ZrO<sub>2</sub> beads. The anode, 15 μm membrane, and cathode were hot pressed for 3 min at 155 °C and 4 kN. A Freudenberg H14C7 carbon fiber paper (Freudenberg & Co. KG, Germany) served as the gas diffusion layer. To record CO stripping voltammograms, the cell was purged with 10% CO in N<sub>2</sub> for ~10 min at a constant potential of 0.1 V, followed by purging with pure N<sub>2</sub> to remove excess CO. The voltammograms were recorded at a scan rate of 100 mV/s. Differential flow H<sub>2</sub>/O<sub>2</sub> (2000 nccm/5000 nccm) polarization curves were recorded at 80 °C, 170 kPa<sub>abs</sub>, and 100% relative humidity. The ohmic resistance was determined via electrochemical impedance spectroscopy. The H<sub>2</sub> crossover was determined under an H<sub>2</sub>/N<sub>2</sub> atmosphere.

**Positron Annihilation Spectroscopy.** For the present study, coincident Doppler broadening spectroscopy (CDBS) was performed at the CDB spectrometer using the monoenergetic positron beam at NEPOMUC located at the research neutron source Heinz Maier Leibnitz (FRM II).<sup>27</sup> The positron implantation energy was varied between 0.10 and 30 keV.<sup>28,29</sup> In order to examine the near surface region, small energy steps of 0.10 and 0.20 keV were chosen up to an implantation energy of 8 keV. The energy of the emitted annihilation radiation was recorded by high purity Ge detectors with a typical energy resolution of 1.30 keV at 511 keV. For the calculation of the *S* parameter the central energy interval was set to 511 ± 0.85 keV. The CDB spectra were recorded at a positron implantation energy of 0.4 keV, where the contribution of the Si substrate can be neglected according to the calculated Makhov profile. The preparation of the samples was performed by dispersing 10 mg of Pt/C<sub>TD</sub> and commercial Pt/C<sub>TKK</sub> catalyst powder in 1 mL of ethanol via sonication. The as prepared inks were drop casted onto a silicon wafer, followed by drying of the sample at 60 °C for 1 h.

#### WAXS Measurements and Rietveld Refinement.

WAXS patterns of Pt/C<sub>TD</sub> and the commercial Pt/C<sub>TKK</sub> were measured at the ID31 beamline of the European synchrotron radiation facility (ESRF, Grenoble, France). High energy X ray radiation of 70 keV was focused on the catalyst powder contained either in a Kapton tape (powder film removed from a rotating disk electrode) or Kapton capillary for Pt/C<sub>TD</sub> and commercial Pt/C<sub>TKK</sub>, respectively. The scattered signal was collected using a Dectris Pilatus CdTe 2 M detector within 5 s exposure time. The 2D signal was azimuthally integrated and reduced to a 1D curve using the pyFAI software package<sup>30</sup> after the energy, detector distance, and tilt were calibrated using a standard CeO<sub>2</sub> powder. The lattice parameter, crystallite size, and microstrain values for the electrocatalysts were estimated by Rietveld refinement of the WAXS patterns using an *Fm3m* structure of metallic Pt and the Fullprof software.<sup>31</sup> Due to an external pollution by Ni, an additional Ni phase was added to refine Pt/C<sub>TD</sub>. The instrument resolution function was determined from the CeO<sub>2</sub> standard WAXS pattern, and the peak shape and the background were described using the Thompson–Cox–Hastings (TCH) function and a polynomial function, respectively. A possibility for a uniaxial anisotropic description

of nanoparticle size along the [111] direction axis was also implemented.

## RESULTS AND DISCUSSION

During the top down synthesis process (see Figure 1A), Pt wires are exposed to strongly polarizing, alternating voltages. Thereby, nanoparticles can be rapidly eroded from the wire surface and subsequently be released into the electrolyte. Due to the rough conditions of our synthetic route, we assume to produce a wide variety of nanoparticle shapes, including surface concavities, combined with the introduction of local strain. In order to investigate the surface defective character of Pt/C<sub>TD</sub>, five different approaches were exploited:

1. HR (S)TEM was used to visualize certain defective surface sites of unsupported Pt<sub>TD</sub> nanoparticles.
2. STEM HAADF tomography visualization was performed to obtain 3D information about the disordered surface regions of unsupported Pt<sub>TD</sub> nanoparticles.
3. PAS was employed to compare the defect concentration of Pt/C<sub>TD</sub> to commercial Pt/C<sub>TKK</sub> (detailed information about the reference catalyst is given in the Experimental Section).
4. Rietveld refinement of WAXS measurements was performed to investigate and quantitatively compare the defect induced degree of microstrain of Pt/C<sub>TD</sub> to commercial Pt/C<sub>TKK</sub>.
5. Electroanalytical methods were used to monitor and compare structural defects and activities of both samples.

In Figure 1B–I, unsupported Pt single nanoparticles are characterized with the use of HR TEM and HR STEM imaging. The images reveal a nonspherical structure of the nanoparticles produced. Indeed, several concave shaped surface regions can be found, as highlighted by red arrows. In detail, several complex shapes of the nanoparticles were found, as is demonstrated by two nanoparticles imaged by the HR STEM HAADF technique in Figure 1B,E, where smaller concavities in the order of few crystal lattice planes and a sharp, deep concavity were revealed. These defects are highlighted in Figure 1C,F, respectively, where a Fourier filtering was used to reduce noise in the original HR STEM images to improve visibility of the atomic structure details. FFT patterns of both nanoparticles (Figure 1D,G), which were obtained from the original HR STEM images, show spots corresponding to platinum {111} and {002} lattice planes with spacings of 0.227 and 0.196 nm, respectively,<sup>32</sup> and a crystal orientation of the nanoparticles to zone axis [110] of the face centered cubic (FCC) lattice. The nanoparticle in Figure 1B was found to be a pure single crystal, while in the case of the nanoparticle in Figure 1E a twinned structure was revealed by FFT. The FFT in Figure 1G shows two [110] FCC zone axis patterns (marked by lattice indexes A and B and by dotted and dashed lines), which are rotated with respect to each other around the common {111} twin plane. Hand in hand with this finding, twinning of the nanoparticle by two corresponding planes of the {111} type was identified, which divides the crystal into three twin grains A, B and B', as is marked in Figure 1F. In addition, the complex shape of the nanoparticles can be seen from a variation in contrast within both crystals imaged by the HR STEM HAADF technique in Figure 1B,E. The resulting contrast under the imaging conditions used is predominantly dependent on the atomic number *Z* and thickness of the sample.<sup>33</sup> As the studied nanoparticles are pure

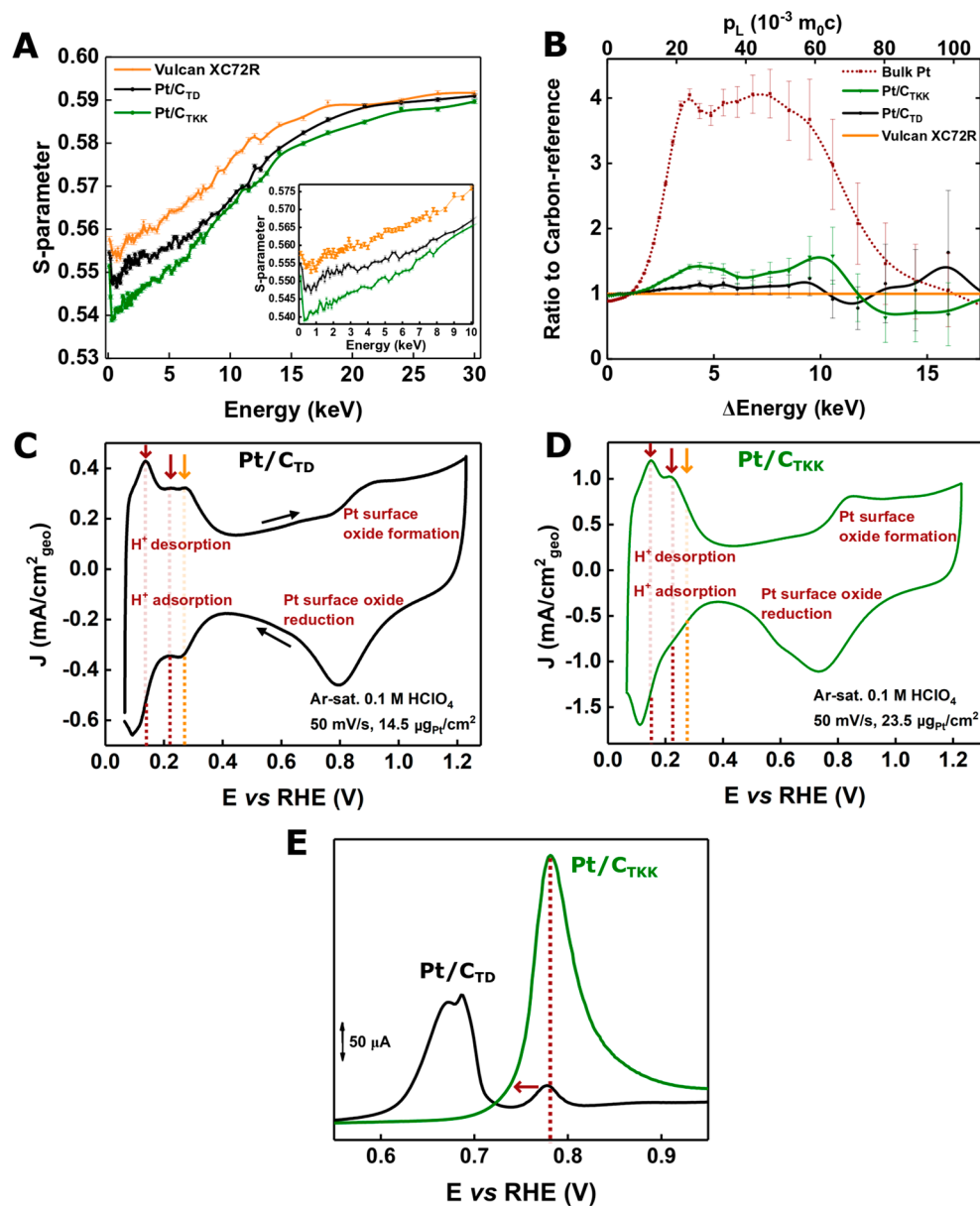


**Figure 2.** (A)  $S$  parameter as a function of the positron implantation energy obtained from DBS measurement. Near the surface, i.e., at low implantation energies, Pt/C<sub>TD</sub> shows a significantly higher  $S$  parameter in comparison to commercial Pt/C<sub>TKK</sub>. The higher  $S$  parameter is mainly attributed to the higher defect concentration of Pt/C<sub>TD</sub>. The inset shows a magnified energy range of 0–10 keV. (B) Ratio curves normalized to the curve of the carbon reference obtained by CDBS. Pt/C<sub>TD</sub> shows a much lower Pt signature (7.5%) in comparison to its commercial counterpart (18.2%). Hence, the positron annihilation probability with Pt core electrons is significantly decreased in Pt/C<sub>TD</sub>, which is ascribed to a higher concentration of defects. (C, D) Typical CVs of Pt/C<sub>TD</sub> and commercial Pt/C<sub>TKK</sub>, respectively (electrolyte, Ar saturated 0.1 M HClO<sub>4</sub>; scan rate, 50 mV/s). Red arrows indicate typical H<sub>UPD</sub> peak positions of Pt/C<sub>TKK</sub>. Pt/C<sub>TD</sub> shows an additional peak shoulder (orange arrow), which indicates the presence of surface structural defects (see main text). (E) CO stripping peaks of Pt/C<sub>TD</sub> (black curve) and commercial Pt/C<sub>TKK</sub> (green curve). The peak shift indicates the presence of surface structural defects. It must be noted that the CO stripping voltammograms were recorded separately, using a slightly modified setup (see the [Experimental Section](#)). CO coverage was achieved by bubbling 0.1 M HClO<sub>4</sub> with pure CO for ~6 min while a constant potential of 0.1 V vs RHE was applied. Saturation of the electrolyte with Ar for ~30 min, followed by a subsequent performance of a full CV cycle, further leads to the oxidation of the CO monolayer (scan rate, 20 mV/s).

Pt crystals, the contrast variations must originate from variations in the sample thickness. Therefore, it is also possible to demonstrate the topological complexity of both nanoparticles. Figure 1H,I shows HR TEM images of two Pt nanoparticles with a “strawberry” like shape, including up to three concave surface regions, which can be considered particularly interesting for electrocatalytic applications. To judge the complexity of the nanoparticle shapes in a broader view, a state of the art STEM HAADF tomography technique,

utilized for the visualization of complex 3D samples with high lateral resolution, was performed on unsupported Pt<sub>TD</sub> nanoparticles. The final 3D visualization of top down synthesized single nanoparticles confirms the presence of surface concavities, as it is illustrated by the example in Figure 1J (left). Moreover, it is visible that surface concave regions appear on both smaller particles and larger particles. Even though the unsupported nanoparticles tend to agglomerate, the tomography technique used revealed the irregular shape of

many individual nanoparticles on the surface of a larger nanoparticle cluster, as is illustrated in [Figure 1J](#) (right side). In comparison to the typically spherically shaped commercial Pt nanoparticles such as the reference catalyst,<sup>34–36</sup> the complex shapes of Pt<sub>TD</sub> nanoparticles prefigure an activity increase. However, a representative quantification of the particularly active sites is not possible due to the individual character of each single nanoparticle.

In order to expand the study of single nanoparticles to the whole system, PAS was employed. It was chosen to examine the defective character of Pt/C<sub>TD</sub> in comparison to commercial Pt/C<sub>TKK</sub>. PAS is known as a powerful, nondestructive tool to detect open volume defects, i.e. vacancies or vacancy clusters, in a crystal lattice. Due to the effective trapping of positrons in such crystal defects, the positron is applied as a highly mobile microprobe with outstanding sensitivity to vacancy concentrations as low as 10<sup>-7</sup> in metals.<sup>37</sup> For the present study, a low energy positron beam is required in order to investigate the near surface region of the Pt/C samples. For a better understanding, some elementary parts of PAS will be explained in the following text, whereas further details can be found in the literature.<sup>38,39</sup> After being implanted in a solid, positrons thermalize within picoseconds and can then diffuse quasi freely through the crystal lattice within a diffusion length typically on the order of 100 nm. They eventually annihilate with a core or valence electron either in the unperturbed crystal lattice or after being trapped at defect sites. The positron–electron annihilation leads predominantly to a back to back emission of two 511 keV  $\gamma$  quanta in the center of mass system. These  $\gamma$  quanta are most important for gaining information about defects, as they will be detected during the experiment. In the laboratory system, the longitudinal component of the electron momentum ( $p_L$ ) causes a Doppler shift of the annihilation quanta. The resulting broadened annihilation photo peak, i.e. recorded counts as a function of  $\gamma$  energy, is analyzed in DBS. For quantitative analysis of the line shape, the so called *S* parameter is commonly applied, which is defined as the fraction of counts in a fixed central region around the 511 keV annihilation peak. Since the central part of the annihilation peak is dominated by positrons annihilating preferably with low momentum valence electrons, the *S* parameter increases with an increasing number of vacancies or vacancy clusters.<sup>40</sup> In CDBS, both  $\gamma$  quanta of an annihilation event are detected simultaneously in a collinear detector setup. Due to the effective suppression of the background, the annihilation of high momentum (core) electrons becomes experimentally accessible: i.e., chemical information can be gained from the surrounding of the annihilation site. For evaluation, CDB spectra are normalized, mirrored at 511 keV, and usually divided by a reference spectrum in order to obtain so called ratio curves in which the elemental signatures can be clearly observed.

[Figure 2A](#) shows the *S* parameter as a function of the positron implantation energy, which is a measure of the probed sample depth.<sup>41</sup> Toward high energies (>25 keV), the commercial carbon reference material (Vulcan XC72R) in the form of carbon nanoparticles with a particle size between 30 and 60 nm<sup>42</sup> and both the commercial Pt/C<sub>TKK</sub> and Pt/C<sub>TD</sub> nanoparticles supported on Vulcan carbon approach the same *S* parameter. This is expected, since at higher energy the positrons are implanted with a higher implantation depth: i.e., most of the positrons are annihilated in the Si substrate. At low energies (<20 keV), the carbon reference possesses a higher *S*

parameter in comparison to both the commercial Pt/C<sub>TKK</sub> and Pt/C<sub>TD</sub>. This can be ascribed to the generally lower *S* parameter of Pt in comparison to the carbon reference, as is also observed in the normalized projection of the CDB spectra ([Figure S1](#)) and the low energy region of the ratio curves ([Figure 2B](#)). More interestingly, on comparison of both samples, Pt/C<sub>TD</sub> shows a significantly higher *S* parameter than commercial Pt/C<sub>TKK</sub>. For an interpretation, it has to be mentioned that Pt/C<sub>TD</sub> and commercial Pt/C<sub>TKK</sub> slightly differ in Pt on carbon weight fraction (TGA) reveals ~15 wt % for Pt/C<sub>TD</sub> and ~20 wt % for the commercial Pt/C<sub>TKK</sub>), whereas the overall Pt loading on the substrate was adjusted. Therefore, due to its slightly smaller Pt content, a slightly higher *S* parameter of Pt/C<sub>TD</sub> in comparison to commercial Pt/C<sub>TKK</sub> was expected. However, the significantly higher *S* parameter of Pt/C<sub>TD</sub> cannot be caused by only the comparably small difference in weight fractions of the samples with similar overall Pt loading. Instead, this effect is attributed to a higher concentration of (open volume) defects in Pt/C<sub>TD</sub> than in commercial Pt/C<sub>TKK</sub>. In order to additionally access the element specific high momentum part of the annihilation line related to core electrons, CDBS was carried out. [Figure 2B](#) shows the ratio curves of Pt/C<sub>TD</sub> and commercial Pt/C<sub>TKK</sub> samples. These ratio curves are obtained by normalization of the individual CDBS raw spectra to the same intensity and subsequent division by a reference spectrum, which is in this case a CDBS spectrum of a carbon reference. For comparison, a spectrum obtained for a bulk Pt reference is shown as well. For both Pt/C<sub>TKK</sub> and Pt/C<sub>TD</sub>, the typical signature of Pt is visible ( $p_L = (10–80) \times 10^{-3} m_0 c$ ). Assuming a simple model that positrons annihilate in either defect free Pt or carbon, one would expect that the respective Pt signal relates to the measured Pt weight fractions (see TGA result above): i.e., the Pt signatures in Pt/C<sub>TD</sub> would amount to 0.75 of that in Pt/C<sub>TKK</sub>. As determined by fitting the curves (see the [Supporting Information](#)), however, the Pt signature in Pt/C<sub>TD</sub> (7.5%) is 0.59 less distinct than in the commercial Pt/C<sub>TKK</sub> (18.2%). Hence, the positron annihilation probability with Pt core electrons is significantly decreased in Pt/C<sub>TD</sub>. This effect is explained by the presence of a higher density of vacancy like defects in Pt/C<sub>TD</sub>, since positrons are likely to be trapped at vacancies, where in turn the annihilation probability with core electrons is reduced. This conclusion is in accordance with the lower density of structural defects in the commercial sample, as observed in the DBS measurements.

Another approach to investigate the presence of structural defects in nanostructured catalysts is the use of high energy X rays. Indeed, recent studies have used Rietveld refinement of WAXS patterns to extract the microstrain (i.e., the local strain) contribution from the experimental Bragg peak broadening.<sup>43–45</sup> Microstrain broadening in diffraction data originates in the local atom displacements from their ideal position, such as those caused by atomic vacancies, stacking faults, or grain boundaries.<sup>46</sup> Here, it should be noted that at the grain boundary of coalescing particles similarly active concave sites are formed. [Figure S2A](#) displays the WAXS pattern measured at the ID31 beamline of the European synchrotron radiation facility (ESRF, Grenoble, France), including the calculated patterns for the Pt/C<sub>TD</sub> catalyst (details about the WAXS pattern of the commercial Pt/C<sub>TKK</sub> catalyst are available in [Figure S2B](#)). The results shown in [Table S1](#) unambiguously support the conclusions obtained from DBS measurements: while commercial Pt/C<sub>TKK</sub> features a zero value of microstrain,

a value of 0.60% is found for Pt/C<sub>TD</sub> (being comparable to or higher than that of some PtNi alloyed samples),<sup>45</sup> confirming its highly defective structure. The resulting surface distortion (SD) value was derived as  $3.9 \pm 0.2\%$  for the synthesized Pt/C<sub>TD</sub> (for further information see ref 45). It should be noted that both techniques are not solely surface sensitive but partially also include bulk information.

Electrochemical measurements further validate the presence of structural surface defects. Figure 2C,D shows typical cyclic voltammograms (CVs) of Pt/C<sub>TD</sub> and commercial Pt/C<sub>TKK</sub>, respectively. In both cases, in the potential range of  $\sim 0.05$ – $0.40$  V vs the reversible hydrogen electrode (RHE), typical hydrogen adsorption and desorption ( $H_{\text{ads/des}}$ ) features of polycrystalline Pt are visible. In detail, commercial Pt/C<sub>TKK</sub> depicts a sharp peak doublet with maxima at  $\sim 0.15$  and  $\sim 0.22$  V vs RHE (red dotted lines). According to Vidal Iglesias et al., using HClO<sub>4</sub> as an electrolyte, features in the range between 0.09 and 0.22 V vs RHE can be ascribed to the  $H_{\text{ads/des}}$  on Pt(110) facets, while the effect of (111) and (100) facets cannot be clearly attributed.<sup>47</sup> In contrast, Pt/C<sub>TD</sub> shows an additional distinct peak shoulder at  $\sim 0.27$  V vs RHE (orange dotted line), which can be assigned to the  $H_{\text{ads/des}}$  on defective surface structures, as proposed by Chattot et al.<sup>44</sup> Herein, we assume that the broad  $H_{\text{des}}$  peak structure provides further evidence for the presence of structural defects on the Pt<sub>TD</sub> nanoparticle surface.

CO stripping voltammograms of both commercial Pt/C<sub>TKK</sub> and Pt/C<sub>TD</sub> are shown in Figure 2E. While the commercial Pt/C only shows a single peak at a potential of  $\sim 0.78$  V vs RHE, indicating mainly isolated, well distributed nanoparticles, Pt/C<sub>TD</sub> shows a peak doublet with maxima located at  $\sim 0.67$  and  $\sim 0.69$  V vs RHE and a singlet at a potential slightly lower than 0.78 V vs RHE. On the basis of the findings of Maillard et al., the appearance of the peak doublet structure at lower potentials can be traced back to the presence of highly defective grain boundaries.<sup>44,48</sup> Recently, Chattot et al. compared the ratio between charge  $Q$  derived from  $\text{CO}_{\text{ads}}$  and  $H_{\text{ads/des}}$  peaks with the level of SD of different Pt based ORR nanocatalysts, indicating a quasi linear relationship.<sup>49</sup> When the proposed evaluation protocols are taken into account, the Pt/C<sub>TD</sub> catalyst shows a  $Q_{\text{CO}}/2Q_{\text{H}}$  ratio of  $0.85 \pm 0.4$ , which indicates a high density of surface defects and is comparable to that of, e.g., hollow PtNi/C.

Previously mentioned observations can be further validated by observations derived from TEM imaging, as depicted in Figure 3A. Indeed, several small Pt nanoparticle agglomerates can be observed. Overall, the Pt nanoparticles are homogeneously distributed on Vulcan carbon; however, the Pt nanoparticle density partially varies. The image shows that, next to particles in the size range of 3–6 nm, several smaller particles with diameter  $\leq 2$  nm can be observed. The corresponding particle size distribution (PSD) from the investigation of 125 isolated nanoparticles is given in Figure 3B, taking into account both edges of each individual particle and no particle agglomerates. PSD analysis was performed using the ImageJ software. On the basis of the broad size distribution, the number averaged ( $d_{\text{N}}$ ) and surface averaged ( $d_{\text{S}}$ ) diameters of the isolated Pt nanoparticles were determined to be  $\sim 3.2 \pm 1.0$  and  $\sim 3.4$  nm, respectively. In the case of the commercial Pt/C<sub>TKK</sub> sample used, a number averaged diameter of  $\sim 2.8 \pm 0.8$  nm can be found in the literature.<sup>50</sup> In contrast to the mean size determined from TEM, WAXS shows a global average size of 8.3 nm (Table S1),

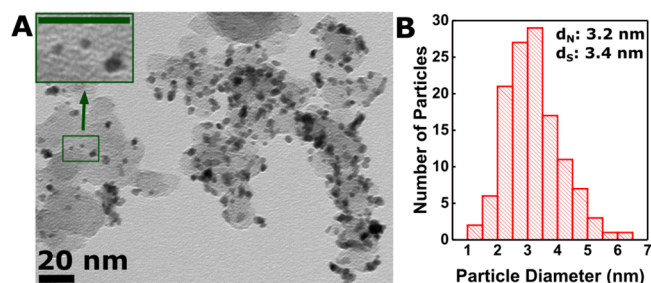


**Figure 3.** (A) TEM image of Pt/C<sub>TD</sub>. The image reveals a homogeneous Pt nanoparticle coverage of the carbon support; however, parts of the support are less densely covered than others. The inset shows a magnification of some particles marked by a green frame (green scale bar, 20 nm). (B) Corresponding PSD of Pt/C<sub>TD</sub>, revealing a number averaged diameter ( $d_{\text{N}}$ ) of  $\sim 3.2 \pm 1.0$  nm and a surface averaged diameter ( $d_{\text{S}}$ ) of  $\sim 3.4$  nm. The PSD was derived from the investigation of 125 isolated Pt nanoparticles.

which indicates a bimodal size distribution consisting of smaller, isolated nanoparticles and larger particle aggregates. Similar observations have previously been reported by Chattot et al., where the partially aggregated A Pt/C electrocatalyst showed a TEM derived mean particle size of 3.4 nm, while WAXS revealed a global average size of 7.4 nm.<sup>45</sup>

In order to evaluate the electrocatalytic activity of Pt/C<sub>TD</sub> toward the ORR, RDE measurements of freshly prepared catalyst inks were conducted. A typical polarization curve of Pt/C<sub>TD</sub> is depicted in Figure 4A. Evaluation of the kinetic current was performed using the Koutecký–Levich equation (eq 1)

$$I_{\text{kin}} = |I \times I_{\text{lim}}| / |I_{\text{lim}} - I| \quad (1)$$

with  $I$  being the measured current,  $I_{\text{kin}}$  being the kinetic current, and  $I_{\text{lim}}$  being the O<sub>2</sub> diffusion limited current of the polarization curve. The kinetic current curve extracted from the polarization curve in the range 0.85–1.0 V is shown in the inset of Figure 4A. The corresponding analysis of commercial Pt/C<sub>TKK</sub> is depicted in Figure S3. As described earlier, due to the high concentration of surface structural defects of Pt/C<sub>TD</sub>, we predict an activity increase in comparison to commercial Pt/C. Indeed, at 0.90 V vs RHE, we observe an  $\sim 3.6$  times enhanced mass activity ( $\sim 712 \pm 20$  mA/mg<sub>Pt</sub>) and an  $\sim 6.8$  times enhanced specific activity ( $\sim 1.62 \pm 0.32$  mA/cm<sub>2</sub><sub>Pt</sub>) of Pt/C<sub>TD</sub> in comparison to commercial Pt/C<sub>E-tek</sub> (activity values taken from the literature),<sup>51,52</sup> and an  $\sim 1.7$  times mass activity and an  $\sim 2.7$  times specific activity enhancement in comparison to Pt/C<sub>TKK</sub>. The activities of Pt/C<sub>TKK</sub> are in good agreement with literature values for the same catalyst, considering the effect of the ionomer concentration.<sup>53</sup> This is a significant improvement over typically used Pt/C electrocatalysts, especially as the activity is compared to one of the most active commercial Pt/C catalysts. Moreover, the activity is even comparable to that of some well known PtNi and PtCo alloyed electrocatalysts.<sup>54,55</sup>

With regard to the stability of Pt/C<sub>TD</sub>, preliminary accelerated durability tests of Pt/C<sub>TKK</sub> and Pt/C<sub>TD</sub> were conducted in the RDE configuration. After 10000 cycles between 0.6 and 1.0 V vs RHE, performed at 80 °C, Pt/C<sub>TD</sub> still shows higher activity in comparison to Pt/C<sub>TKK</sub> (Figure S4A). As expected, post mortem TEM analysis of Pt/C<sub>TD</sub> shows strong particle sintering at elevated temperature.

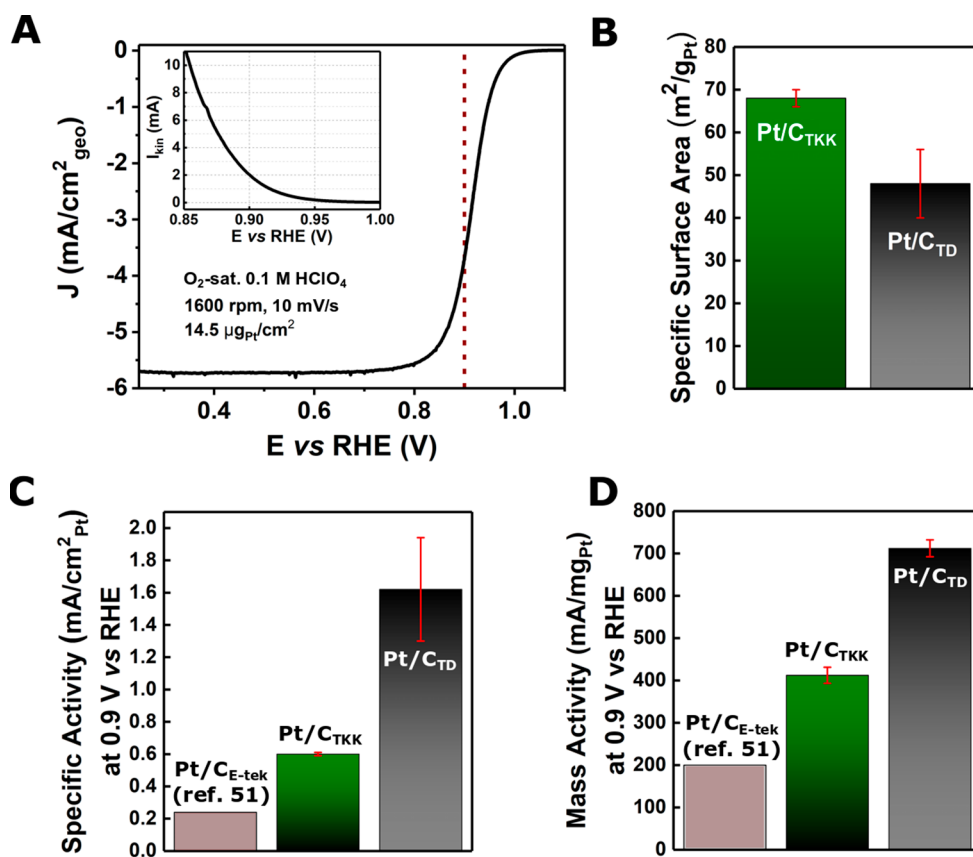


**Figure 4.** (A) Typical  $iR$  corrected polarization curve of Pt/C<sub>TD</sub> (anodic scan; electrolyte, O<sub>2</sub> saturated 0.1 M HClO<sub>4</sub>; scan rate, 10 mV/s; rotational speed, 1600 rpm). Pseudocapacitive currents were corrected by subtraction of a background CV. The measurement is normalized to the geometrical area of the glassy carbon electrode used in the experiments (0.196 cm<sup>2</sup>), and an electrode loading of  $\sim 14.5 \mu\text{g}_{\text{Pt}}/\text{cm}^2$  was adjusted. The corresponding kinetic current curve in the potential range 0.85–1.00 V vs RHE is displayed in the inset of the graph. (B) SSA of Pt/C<sub>TD</sub> compared to the SSA of commercial Pt/C<sub>TKK</sub>. (C) Specific activity of Pt/C<sub>TD</sub> compared to those of commercial Pt/C<sub>E-tek</sub> (activity value taken from ref 51, benchmarked under similar conditions) and Pt/C<sub>TKK</sub> at 0.9 V vs RHE. (D) Mass activity of Pt/C<sub>TD</sub> compared to those of commercial Pt/C<sub>E-tek</sub> (activity value taken from ref 51, benchmarked under similar conditions) and Pt/C<sub>TKK</sub> at 0.9 V vs RHE.

Moreover, isolated particles appear to become more spherical (Figure S4B).

To determine the specific activity of Pt/C<sub>TD</sub>, the kinetic current at 0.90 V vs RHE was normalized to the electrochemically active surface area (ECSA) of the catalyst. Integration of the H<sub>UPD</sub> charge of each CV was used to determine the ECSA. For the adsorption and desorption of a monolayer of H on Pt, a charge density of 210  $\mu\text{C}/\text{cm}^2_{\text{Pt}}$  was assumed. The determination of the mass activity was conducted by normalizing the kinetic current to the Pt mass deposited on the working electrode.

The specific surface area (SSA) of Pt/C<sub>TD</sub> was determined to be  $\sim 46 \pm 8 \text{ m}^2/\text{g}_{\text{Pt}}$  while commercial Pt/C<sub>TKK</sub> exhibits an SSA of  $\sim 68 \pm 2 \text{ m}^2/\text{g}_{\text{Pt}}$  (being comparable to literature data, considering the effect of the ionomer concentration).<sup>53</sup> In both cases, the SSA was normalized to the catalyst mass deposited on the working electrode. When comparing the average sizes of both catalysts, only a slightly reduced SSA in comparison to Pt/C<sub>TKK</sub> is expected. Hence, we assume that the actual difference in SSA is partially caused by agglomeration of the Pt nanoparticles, as can be seen in Figure 3A. The activity data and SSA values of Pt/C<sub>TD</sub> and commercial Pt/C are compared in Figure 4B–D.

To further investigate the performance of Pt/C<sub>TD</sub> in an actual membrane electrode assembly (MEA), preliminary measurements in a single cell PEMFC were conducted. To

meet current industrial targets to produce PEMFCs with low Pt content, MEAs with a cathode loading of  $\sim 0.1 \text{ mg}_{\text{Pt}}/\text{cm}^2$  were prepared and examined. The results are shown in Figure 5. Figure 5A depicts the CO stripping voltammogram of the Pt/C<sub>TD</sub> catalyst layer. As observed in the RDE measurements, the voltammogram shows a characteristic double peak between 0.6 and 0.9 V, associated with surface defects. Evaluation of the SSA gives a value of  $\sim 26.5 \text{ m}^2/\text{g}_{\text{Pt}}$ , this being  $\sim 40\%$  lower than the values measured in the RDE tests (assumed standard charge of a CO monolayer on Pt: 420  $\mu\text{C}/\text{cm}^2$ ). This observation could be due to the increased catalyst batch size, leading to stronger agglomeration of the Pt nanoparticles, or to nonuniform ionomer wetting of the catalyst layer in the MEA. The ORR kinetics of Pt/C<sub>TD</sub> were extracted from the H<sub>2</sub>/O<sub>2</sub> polarization curves after correction of the  $iR$  drop and the H<sub>2</sub> crossover. At 0.9 V, a noticeable increase in the mass activity in comparison to Pt/C<sub>TKK</sub> (Figure 5B,C; reference data measured in the same setup under identical conditions were taken from the literature<sup>56</sup>) can be observed, validating the results obtained from RDE studies. Owing to the so called particle size effect, the specific activity of both catalysts is poorly comparable, as the SSA of Pt/C<sub>TKK</sub> is more than 2.5 times larger than the SSA of Pt/C<sub>TD</sub>.<sup>56,57</sup> Hence, in order to compare the intrinsic activity of Pt/C<sub>TD</sub>, we included the activity data of heat treated Pt/C<sub>TKK</sub> recorded by Schwämmlein et al. (HT Pt/C<sub>TKK</sub>, taken from the literature<sup>56</sup>) with an SSA of  $\sim 7 \text{ m}^2/$

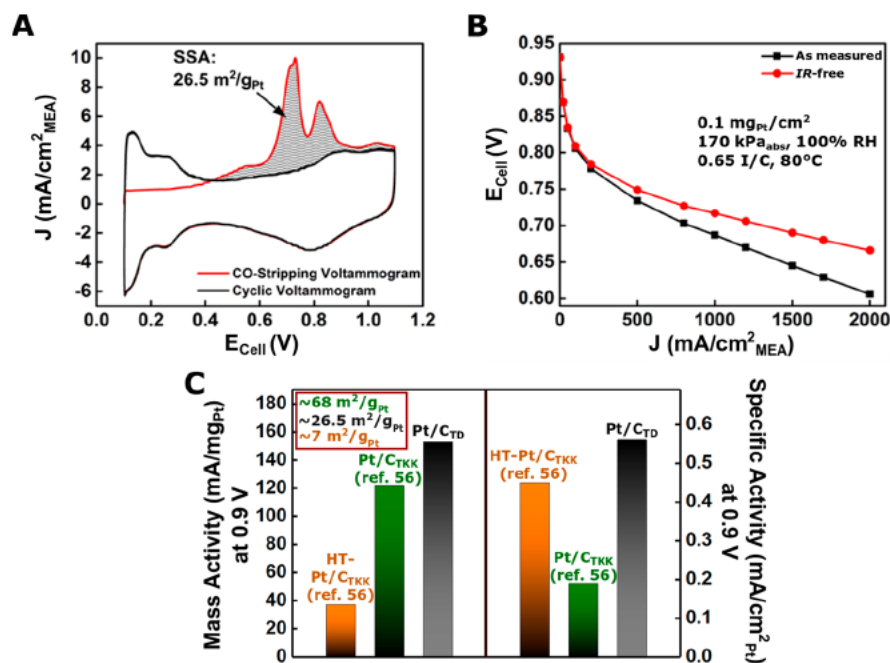


**Figure 5.** (A) CO stripping voltammogram of the Pt/C<sub>TD</sub> cathode catalyst layer, showing a characteristic double peak. Integration of the peaks and normalization to Pt mass leads to a SSA of  $\sim 26.5 \text{ m}^2/\text{g}_{\text{Pt}}$ . (B) Uncorrected and *iR* corrected H<sub>2</sub>/O<sub>2</sub> differential flow polarization curve of the Pt/C<sub>TD</sub> based MEA (0.1 mg<sub>Pt</sub>/cm<sup>2</sup>, 0.65 I/C ratio), recorded at a pressure of 170 kPa<sub>abs</sub>, 80 °C, and 100% relative humidity (RH). (C) Mass and specific activities of Pt/C<sub>TD</sub> at 0.9 V, in comparison to Pt/C<sub>TKK</sub> (SSA  $\sim 68 \text{ m}^2/\text{g}_{\text{Pt}}$ ) and heat treated Pt/C<sub>TKK</sub> (SSA  $\sim 7 \text{ m}^2/\text{g}_{\text{Pt}}$ ). For activity evaluation, the H<sub>2</sub>/O<sub>2</sub> data were corrected for the *iR* drop and the H<sub>2</sub> crossover current. The reference data were taken from ref 56; however, the catalyst was examined in the same setup and under identical conditions.

g<sub>Pt</sub>. Due to the smaller SSA of HT Pt/C<sub>TKK</sub>, higher specific activity is expected. However, at 0.9 V we still observe higher specific activity of Pt/C<sub>TD</sub> in comparison to HT Pt/C<sub>TKK</sub>, indicating the higher intrinsic activity of Pt/C<sub>TD</sub>. While at 0.9 V only kinetic losses are expected, at higher current densities the low roughness factor (cm<sup>2</sup><sub>Pt</sub>/cm<sup>2</sup><sub>MEA</sub>) leads to a poor O<sub>2</sub> mass transport, as previously reported by Harzer, Schwämmlein, et al.<sup>50,56</sup> Here, in particular, proper wetting of the catalyst layer with ionomer has to be ensured in order to prevent losses. Thus, we assume that, for upscaled batch sizes, enhancement of the SSA of Pt/C<sub>TD</sub> through an improved synthesis procedure (e.g., improved mixing of the electrolyte during synthesis) and adjustment of the ionomer distribution could further improve the performance of the catalyst, especially at high current densities. Moreover, in future experimental studies, the stability of defect rich Pt/C<sub>TD</sub> in the MEA setup has to be evaluated, as this task was out of the scope of this work. However, accelerated stress tests of Schwämmlein et al. indicate that, in the MEA, a lower SSA has beneficial effects on the stability of the catalyst, which should be considered prior to adjustment of the surface area.<sup>56</sup>

## CONCLUSIONS

Within this work, we show an upscalable, top down, one pot synthetic approach toward highly active Pt/C electrocatalysts, circumventing typical demanding multistep synthesis procedures. In RDE studies, the synthesized Pt/C<sub>TD</sub> shows high activity toward the ORR with specific and mass activities of 1.62 mA/cm<sup>2</sup><sub>Pt</sub> and 712 mA/mg<sub>Pt</sub>, respectively. An ORR activity enhancement over commercial Pt/C was further confirmed in a single cell PEMFC. On the basis of TEM, WAXS, CV, and PAS experiments, the origin of the superior activity in comparison to commercial Pt/C can be correlated

to the introduction of a high density of surface defects, such as surface concavities. Furthermore, when the high complexity of classical nucleation driven bottom up syntheses and costs of the precursor materials are considered, the top down approach not only facilitates the synthesis but should also save overall processing costs in large scale applications.

## ASSOCIATED CONTENT

### Supporting Information

The Supporting Information is available free of charge at <https://pubs.acs.org/doi/10.1021/acscatal.9b04974>.

Coincident Doppler broadening spectrum, WAXS measurements, Rietveld refinement data, reference ORR polarization curve, accelerated durability test, and TEM analysis (PDF)

## AUTHOR INFORMATION

### Corresponding Author

Aliaksandr S. Bandarenka – *Physics of Energy Conversion and Storage and Catalysis Research Center, Technical University of Munich, 85748 Garching, Germany*; [orcid.org/0000-0002-5970-4315](https://orcid.org/0000-0002-5970-4315); Phone: +49 (0) 89 289 12531; Email: [bandarenka@ph.tum.de](mailto:bandarenka@ph.tum.de)

### Authors

Johannes Fichtner – *Physics of Energy Conversion and Storage, Technical University of Munich, 85748 Garching, Germany*  
 Sebastian Watzele – *Physics of Energy Conversion and Storage, Technical University of Munich, 85748 Garching, Germany*  
 Batyr Garlyyev – *Physics of Energy Conversion and Storage, Technical University of Munich, 85748 Garching, Germany*  
 Regina M. Kluge – *Physics of Energy Conversion and Storage, Technical University of Munich, 85748 Garching, Germany*

Felix Haimerl – Physics of Energy Conversion and Storage, Technical University of Munich, 85748 Garching, Germany

Hany A. El Sayed – Chair of Technical Electrochemistry, Technical University of Munich, 85748 Garching, Germany;

orcid.org/0000 0002 8769 8258

Wei Jin Li – Chair of Inorganic and Metal Organic Chemistry, Technical University of Munich, 85748 Garching, Germany

Frédéric M. Maillard – Univ. Grenoble Alpes, Univ. Savoie Mont Blanc, CNRS, Grenoble INP, LEPMI, 38000 Grenoble, France; orcid.org/0000 0002 6470 8900

Laetitia Dubau – Univ. Grenoble Alpes, Univ. Savoie Mont Blanc, CNRS, Grenoble INP, LEPMI, 38000 Grenoble, France; orcid.org/0000 0001 9520 1435

Raphaël Chattot – ESRF The European Synchrotron, 38043 Grenoble, France

Jan Michalička – Central European Institute of Technology, Brno University of Technology, 612 00 Brno, Czech Republic

Jan M. Macak – Central European Institute of Technology, Brno University of Technology, 612 00 Brno, Czech Republic

Wu Wang – Institute of Nanotechnology, Karlsruhe Institute of Technology, 76344 Eggenstein Leopoldshafen, Germany; Joint Research Laboratory Nanomaterials, Technische Universität Darmstadt, 64287 Darmstadt, Germany

Di Wang – Institute of Nanotechnology, Karlsruhe Institute of Technology, 76344 Eggenstein Leopoldshafen, Germany; Karlsruhe Nano Micro Facility, Karlsruhe Institute of Technology, 76344 Eggenstein Leopoldshafen, Germany; orcid.org/0000 0001 9817 7047

Thomas Gigl – FRM II at Heinz Maier Leibnitz Zentrum (MLZ), Technical University of Munich, 85748 Garching, Germany

Christoph Hugenschmidt – FRM II at Heinz Maier Leibnitz Zentrum (MLZ), Technical University of Munich, 85748 Garching, Germany

## Author Contributions

The manuscript was written through contributions of all authors. All authors have given approval to the final version of the manuscript.

## Author Contributions

▼ J.F. and S.W. contributed equally to this work.

## Notes

The authors declare no competing financial interest.

## ACKNOWLEDGMENTS

We gratefully acknowledge financial support from the Deutsche Forschungsgemeinschaft (DFG, German Research Foundation) under Germany's excellence strategy EXC 2089/1–390776260, Germany's excellence cluster "e conversion", DFG projects BA 5795/4 1 and BA 5795/3 1, and the TUM International Graduate School of Science and Engineering, project 11.01. Support from CEITEC Nano Research Infra structure and Karlsruhe Nano Micro Facility as well as financial support from the Ministry of Youth, Education and Sports of the Czech Republic, projects LM2015041 and LQ1601, are gratefully acknowledged. W.J.L. gratefully acknowledges financial support from the Alexander von Humboldt fellowship for postdoctoral researchers. We thank Prof. Hubert A. Gasteiger for providing reference electrocatalyst samples and for providing access to his fuel cell test equipment. We are

thankful to Jan N. Schwämmlein for conducting the fuel cell test measurements. We thank Prof. Hendrik Dietz for granting access to his transmission electron microscopy facilities.

## REFERENCES

- (1) Thomas, C. E. Fuel Cell and Battery Electric Vehicles Compared. *Int. J. Hydrogen Energy* 2009, 34, 6005–6020.
- (2) Pellow, M. A.; Emmott, C. J. M.; Barnhart, C. J.; Benson, S. M. Hydrogen or Batteries for Grid Storage? A Net Energy Analysis. *Energy Environ. Sci.* 2015, 8, 1938–1952.
- (3) Yoshida, T.; Kojima, K. Toyota MIRAI Fuel Cell Vehicle and Progress Toward a Future Hydrogen Society. *Electrochem. Soc. Interface* 2015, 24, 45–49.
- (4) Chen, S.; Sheng, W.; Yabuuchi, N.; Ferreira, P. J.; Allard, L. A.; Shao Horn, Y. Origin of Oxygen Reduction Reaction Activity on "Pt<sub>3</sub>Co" Nanoparticles: Atomically Resolved Chemical Compositions and Structures. *J. Phys. Chem. C* 2009, 113, 1109–1125.
- (5) Oezaslan, M.; Hasché, F.; Strasser, P. PtCu<sub>3</sub>, PtCu and Pt<sub>3</sub>Cu Alloy Nanoparticle Electrocatalysts for Oxygen Reduction Reaction in Alkaline and Acidic Media. *J. Electrochem. Soc.* 2012, 159, B444–B454.
- (6) Garlyyev, B.; Pohl, M. D.; Čolić, V.; Liang, Y.; Butt, F. K.; Holleitner, A.; Bandarenka, A. S. High Oxygen Reduction Reaction Activity of Pt<sub>3</sub>Pr Electrodes in Acidic Media. *Electrochem. Commun.* 2018, 88, 10–14.
- (7) Stephens, I. E. L.; Bondarenko, A. S.; Grønbjerg, U.; Rossmeisl, J.; Chorkendorff, I. Understanding the Electrocatalysis of Oxygen Reduction on Platinum and its Alloys. *Energy Environ. Sci.* 2012, 5, 6744–6762.
- (8) Kitchin, J. R.; Nørskov, J. K.; Barteau, M. A.; Chen, J. G. Role of Strain and Ligand Effects in the Modification of the Electronic and Chemical Properties of Bimetallic Surfaces. *Phys. Rev. Lett.* 2004, 93, 156801.
- (9) Bligaard, T.; Nørskov, J. K. Ligand Effects in Heterogeneous Catalysis and Electrochemistry. *Electrochim. Acta* 2007, 52, 5512–5516.
- (10) Stamenkovic, V. R.; Fowler, B.; Mun, B. S.; Wang, G.; Ross, P. N.; Lucas, C. A.; Marković, N. M. Improved Oxygen Reduction Activity on Pt<sub>3</sub>Ni(111) via Increased Surface Site Availability. *Science* 2007, 315, 493–497.
- (11) Zhang, J.; Yang, H.; Fang, J.; Zou, S. Synthesis and Oxygen Reduction Activity of Shape Controlled Pt<sub>3</sub>Ni Nanopolyhedra. *Nano Lett.* 2010, 10, 638–644.
- (12) Mi, S.; Cheng, N.; Jiang, H.; Li, C.; Jiang, H. Porous Pt<sub>3</sub>Ni with Enhanced Activity and Durability Towards Oxygen Reduction Reaction. *RSC Adv.* 2018, 8, 15344–15351.
- (13) Durst, J.; Chatenet, M.; Maillard, F. Impact of Metal Cations on the Electrocatalytic Properties of Pt/C Nanoparticles at Multiple Phase Interfaces. *Phys. Chem. Chem. Phys.* 2012, 14, 13000–13009.
- (14) Garlyyev, B.; Kratzl, K.; Rück, M.; Michalička, J.; Fichtner, J.; Macak, J. M.; Kratky, T.; Günther, S.; Cokoja, M.; Bandarenka, A. S.; Gagliardi, A.; Fischer, R. A. Optimizing the Size of Platinum Nanoparticles for Enhanced Mass Activity in the Electrochemical Oxygen Reduction Reaction. *Angew. Chem., Int. Ed.* 2019, 58, 9596–9600.
- (15) Dubau, L.; Asset, T.; Chattot, R.; Bonnaud, C.; Vanpeene, V.; Nelayah, J.; Maillard, F. Tuning the Performance and the Stability of Porous Hollow PtNi/C Nanostructures for the Oxygen Reduction Reaction. *ACS Catal.* 2015, 5, 5333–5341.
- (16) Henning, S.; Kühn, L.; Herranz, J.; Durst, J.; Binninger, T.; Nachttegaal, M.; Werheid, M.; Liu, W.; Adam, M.; Kaskel, S.; Eychmüller, A.; Schmidt, T. J. Pt Ni Aerogels as Unsupported Electrocatalysts for the Oxygen Reduction Reaction. *J. Electrochem. Soc.* 2016, 163, F998–F1003.
- (17) Calle Vallejo, F.; Pohl, M. D.; Reinisch, D.; Loffreda, D.; Sautet, P.; Bandarenka, A. S. Why Conclusions from Platinum Model Surfaces Do Not Necessarily Lead to Enhanced Nanoparticle

Catalysts for the Oxygen Reduction Reaction. *Chem. Sci.* **2017**, *8*, 2283–2289.

(18) Calle Vallejo, F.; Tymoczko, J.; Colic, V.; Vu, Q. H.; Pohl, M. D.; Morgenstern, K.; Loffreda, D.; Sautet, P.; Schuhmann, W.; Bandarenka, A. S. Finding Optimal Surface Sites on Heterogeneous Catalysts by Counting Nearest Neighbors. *Science* **2015**, *350*, 185–189.

(19) Yu, T.; Kim, D. Y.; Zhang, H.; Xia, Y. Platinum Concave Nanocubes with High Index Facets and Their Enhanced Activity for Oxygen Reduction Reaction. *Angew. Chem., Int. Ed.* **2011**, *50*, 2773–2777.

(20) Chen, A.; Holt Hindle, P. Platinum Based Nanostructured Materials: Synthesis, Properties, and Applications. *Chem. Rev.* **2010**, *110*, 3767–3804.

(21) Bredig, G.; Haber, F. Ueber Zerstäubung von Metallkathoden bei der Elektrolyse mit Gleichstrom. *Ber. Dtsch. Chem. Ges.* **1898**, *31*, 2741–2752.

(22) Yanson, A. I.; Rodriguez, P.; Garcia Araez, N.; Mom, R. V.; Tichelaar, F. D.; Koper, M. T. M. Cathodic Corrosion: A Quick, Clean, and Versatile Method for the Synthesis of Metallic Nano particles. *Angew. Chem., Int. Ed.* **2011**, *50*, 6346–6350.

(23) Feng, J.; Chen, D.; Sediq, A. S.; Romeijn, S.; Tichelaar, F. D.; Jiskoot, W.; Yang, J.; Koper, M. T. M. Cathodic Corrosion of a Bulk Wire to Nonaggregated Functional Nanocrystals and Nanoalloys. *ACS Appl. Mater. Interfaces* **2018**, *10*, 9532–9540.

(24) Huang, W.; Chen, S.; Zheng, J.; Li, Z. Facile Preparation of Pt Hydrosols by Dispersing Bulk Pt with Potential Perturbations. *Electrochem. Commun.* **2009**, *11*, 469–472.

(25) Chen, X.; Chen, S.; Huang, W.; Zheng, J.; Li, Z. Facile Preparation of Bi Nanoparticles by Novel Cathodic Dispersion of Bulk Bismuth Electrodes. *Electrochim. Acta* **2009**, *54*, 7370–7373.

(26) Fichtner, J.; Garlyyev, B.; Watzele, S.; El Sayed, H. A.; Schwämmlein, J. N.; Li, W.; Maillard, F.; Dubau, L.; Michalička, J.; Macak, J.; Holleitner, A.; Bandarenka, A. S. Top Down Synthesis of Nanostructured Platinum Lanthanide Alloy Oxygen Reduction Reaction Catalysts: Pt<sub>3</sub>Pr/C as an Example. *ACS Appl. Mater. Interfaces* **2019**, *11*, 5129–5135.

(27) Hugenschmidt, C.; Löwe, B.; Mayer, J.; Piochacz, C.; Pikart, P.; Repper, R.; Stadlbauer, M.; Schreckenbach, K. Unprecedented Intensity of a Low Energy Positron Beam. *Nucl. Instrum. Methods Phys. Res., Sect. A* **2008**, *593*, 616–618.

(28) Gigl, T.; Beddrich, L.; Dickmann, M.; Rienäcker, B.; Thalmayr, M.; Vohburger, S.; Hugenschmidt, C. Defect Imaging and Detection of Precipitates Using a New Scanning Positron Microbeam. *New J. Phys.* **2017**, *19*, 123007.

(29) Hugenschmidt, C.; Ceeh, H.; Gigl, T.; Lippert, F.; Piochacz, C.; Pikart, P.; Reiner, M.; Weber, J.; Zimnik, S. The Upgrade of the Neutron Induced Positron Source NEPOMUC. *J. Phys.: Conf. Ser.* **2013**, *443*, 012079.

(30) Ashiotis, G.; Deschildre, A.; Nawaz, Z.; Wright, J. P.; Karkoulis, D.; Picca, F. E.; Kieffer, J. The Fast Azimuthal Integration Python Library: PyFAI. *J. Appl. Crystallogr.* **2015**, *48*, 510–519.

(31) Rodríguez Carvajal, J.; Roisnel, T. Line Broadening Analysis Using FullProf<sup>®</sup>: Determination of Microstructural Properties. *Mater. Sci. Forum* **2004**, *443–444*, 123–126.

(32) Davey, W. P. Precision Measurements of the Lattice Constants of Twelve Common Metals. *Phys. Rev.* **1925**, *25*, 753–761.

(33) Nellist, P. D.; Pennycook, S. J. The Principles and Interpretation of Annular Dark Field Z Contrast Imaging. *Adv. Imaging Electron Phys.* **2000**, *113*, 147–203.

(34) Sneed, B. T.; Cullen, D. A.; Reeves, K. S.; Dyck, O. E.; Langlois, D. A.; Mukundan, R.; Borup, R. L.; More, K. L. 3D Analysis of Fuel Cell Electrocatalyst Degradation on Alternate Carbon Supports. *ACS Appl. Mater. Interfaces* **2017**, *9*, 29839–29848.

(35) Mayrhofer, K. J.; Meier, J. C.; Ashton, S. J.; Wiberg, G. K.; Kraus, F.; Hanzlik, M.; Arenz, M. Fuel Cell Catalyst Degradation on the Nanoscale. *Electrochem. Commun.* **2008**, *10*, 1144–1147.

(36) Meier, J. C.; Galeano, C.; Katsounaros, I.; Topalov, A. A.; Kostka, A.; Schüth, F.; Mayrhofer, K. J. Degradation Mechanisms of

Pt/C Fuel Cell Catalysts Under Simulated Start Stop Conditions. *ACS Catal.* **2012**, *2*, 832–843.

(37) Coleman, P. *Positron Beams and Their Applications*, 1st ed.; World Scientific: Singapore, 2000.

(38) Schultz, P. G.; Lynn, K. G. Interaction of Positron Beams with Surfaces, Thin Films, and Interfaces. *Rev. Mod. Phys.* **1988**, *60*, 701–779.

(39) Hugenschmidt, C. Positrons in Surface Physics. *Surf. Sci. Rep.* **2016**, *71*, 547–594.

(40) Krause Rehberg, R.; Leipner, H. S. *Positron Annihilation in Semiconductors: Defect Studies*, 2nd ed.; Springer: Berlin, 2003.

(41) Makhov, A. F. The Penetration of Electrons into Solids. 2. The Distribution of Electrons in Depth. *Sov. Phys. Solid State* **1961**, *2*, 1942–1944.

(42) Sanders, I. J.; Peeten, T. L. *Carbon Black: Production, Properties, and Uses*, 1st ed.; Nova Science: Hauppauge, 2011.

(43) Dubau, L.; Nelayah, J.; Moldovan, S.; Ersen, O.; Bordet, P.; Drnec, J.; Asset, T.; Chattot, R.; Maillard, F. Defects Do Catalysis: CO Monolayer Oxidation and Oxygen Reduction Reaction on Hollow PtNi/C Nanoparticles. *ACS Catal.* **2016**, *6*, 4673–4684.

(44) Chattot, R.; Asset, T.; Bordet, P.; Drnec, J.; Dubau, L.; Maillard, F. Beyond Strain and Ligand Effects: Microstrain Induced Enhancement of the Oxygen Reduction Reaction Kinetics on Various PtNi/C Nanostructures. *ACS Catal.* **2017**, *7*, 398–408.

(45) Chattot, R.; Le Bacq, O.; Beermann, V.; Kühl, S.; Herranz, J.; Henning, S.; Kühn, L.; Asset, T.; Guétaz, L.; Renou, G.; Drnec, J.; Bordet, P.; Pasturel, A.; Eychmüller, A.; Schmidt, T. J.; Strasser, P.; Dubau, L.; Maillard, F. Surface Distortion as a Unifying Concept and Descriptor in Oxygen Reduction Reaction Electrocatalysis. *Nat. Mater.* **2018**, *17*, 827–833.

(46) Qin, W.; Szpunar, J. A. Origin of Lattice Strain in Nanocrystalline Materials. *Philos. Mag. Lett.* **2005**, *85*, 649–656.

(47) Vidal Iglesias, F. J.; Arán Ais, R. M.; Solla Gullón, J.; Herrero, E.; Feliu, J. M. Electrochemical Characterization of Shape Controlled Pt Nanoparticles in Different Supporting Electrolytes. *ACS Catal.* **2012**, *2*, 901–910.

(48) Maillard, F.; Schreier, S.; Hanzlik, M.; Savinova, E. R.; Weinkauff, S.; Stimming, U. Influence of Particle Agglomeration on the Catalytic Activity of Carbon Supported Pt Nanoparticles in CO Monolayer Oxidation. *Phys. Chem. Chem. Phys.* **2005**, *7*, 385–393.

(49) Chattot, R.; Martens, I.; Scohy, M.; Herranz, J.; Drnec, J.; Maillard, F.; Dubau, L. Disclosing Pt Bimetallic Alloy Nanoparticle Surface Lattice Distortion with Electrochemical Probes. *ACS Energy Lett.* **2020**, *5*, 162–169.

(50) Harzer, G. S.; Schwämmlein, J. N.; Damjanovic, A. M.; Ghosh, S.; Gasteiger, H. A. Cathode Loading Impact on Voltage Cycling Induced PEMFC Degradation: A Voltage Loss Analysis. *J. Electrochem. Soc.* **2018**, *165*, F3118–F3131.

(51) Kuttiyil, K. A.; Sasaki, K.; Choi, Y.; Su, D.; Liu, P.; Adzic, R. R. Bimetallic IrNi Core Platinum Monolayer Shell Electrocatalysts for the Oxygen Reduction Reaction. *Energy Environ. Sci.* **2012**, *5*, 5297–5304.

(52) Godínez Salomón, F.; Rhodes, C. P.; Alcantara, K. S.; Zhu, Q.; Canton, S. E.; Calderon, H. A.; Reyes Rodríguez, J. L.; Leyva, M. A.; Solorza Feria, O. Tuning the Oxygen Reduction Activity and Stability of Ni(OH)<sub>2</sub>@Pt/C Catalysts through Controlling Pt Surface Composition, Strain, and Electronic Structure. *Electrochim. Acta* **2017**, *247*, 958–969.

(53) Orfanidi, A.; Madkikar, P.; El Sayed, H. A.; Harzer, G. S.; Kratky, T.; Gasteiger, H. A. The Key to High Performance Low Pt Loaded Electrodes. *J. Electrochem. Soc.* **2017**, *164*, F418–F426.

(54) Mezzavilla, S.; Baldizzone, C.; Swertz, A. C.; Hodnik, N.; Pizzutilo, E.; Polymeros, G.; Keeley, G. P.; Knossalla, J.; Heggen, M.; Mayrhofer, K. J. J.; Schüth, F. Structure Activity Stability Relationships for Space Confined Pt<sub>3</sub>Ni<sub>y</sub> Nanoparticles in the Oxygen Reduction Reaction. *ACS Catal.* **2016**, *6*, 8058–8068.

(55) Pizzutilo, E.; Knossalla, J.; Geiger, S.; Grote, J. P.; Polymeros, G.; Baldizzone, C.; Mezzavilla, S.; Ledendecker, M.; Mingers, A.; Cherevko, S.; Schüth, F.; Mayrhofer, K. J. J. The Space Confinement

Approach Using Hollow Graphitic Spheres to Unveil Activity and Stability of Pt Co Nanocatalysts for PEMFC. *Adv. Energy Mater.* **2017**, *7*, 1700835.

(56) Schwämmlein, J. N.; Harzer, G. S.; Pfändner, P.; Blankenship, A.; El Sayed, H. A.; Gasteiger, H. A. Activity and Stability of Carbon Supported Pt<sub>x</sub>Y Alloys for the ORR Determined by RDE and Single Cell PEMFC Measurements. *J. Electrochem. Soc.* **2018**, *165*, J3173–J3185.

(57) Nesselberger, M.; Ashton, S.; Meier, J. C.; Katsounaros, I.; Mayrhofer, K. J. J.; Arenz, M. The Particle Size Effect on the Oxygen Reduction Reaction Activity of Pt Catalysts: Influence of Electrolyte and Relation to Single Crystal Models. *J. Am. Chem. Soc.* **2011**, *133*, 17428–17433.